

Study of flow-plane decorrelations in heavy-ion collisions with multiple-plane cumulants

Zhiwan Xu,^{1,*} Xiatong Wu,¹ Caleb Sword,² Gang Wang,^{1,†} Sergei A. Voloshin,² and Huan Zhong Huang^{1,3}

¹*Department of Physics and Astronomy, University of California, Los Angeles, California 90095, USA*

²*Department of Physics and Astronomy, Wayne State University, 666 W. Hancock, Detroit, Michigan 48201*

³*Key Laboratory of Nuclear Physics and Ion-beam Application (MOE),*

and Institute of Modern Physics, Fudan University, Shanghai-200433, People's Republic of China

The azimuthal correlations between local flow planes at different (pseudo)rapidities (η) may reveal important details of the initial nuclear matter density distributions in heavy-ion collisions. Extensive experimental measurements of a factorization ratio (r_2) and its derivative (F_2) have shown evidence of the longitudinal flow-plane decorrelation. However, nonflow effects also affect this observable and prevent a quantitative understanding of the phenomenon. In this paper, to distinguish decorrelation and nonflow effects, we propose a new cumulant observable, T_2 , which largely suppresses nonflow. The technique sensitivity to different initial-state scenarios and nonflow effects are tested with a simple Monte Carlo model, and in the end, the method is applied to events simulated by a multiphase transport model (AMPT) for Au+Au collisions at $\sqrt{s_{NN}} = 200$ GeV.

keywords: flow decorrelation, nonflow

I. INTRODUCTION

Experiments on high-energy heavy-ion collisions, such as those at the Relativistic Heavy Ion Collider (RHIC) and the Large Hadron Collider (LHC), aim to create a quark gluon plasma (QGP) and to study the properties of this deconfined nuclear medium. Most heavy-ion collisions are not head-on, and traditionally, the nucleons experiencing at least one collision are considered as participants, and the remaining are labeled as spectators (see Fig. 1). While spectators fly away, the system created by the participant interaction presumably undergoes a hydrodynamic expansion. The initial geometry of the system is determined by the participant distribution, with event-by-event fluctuations. The pressure gradients of the medium convert the spatial anisotropies of the initial matter distribution into the momentum anisotropies of the final-state particles. Consequently, the azimuthal distributions of emitted particles can be analyzed with a Fourier expansion [1, 2]

$$\frac{dN}{d\varphi} \propto 1 + \sum_{n=1}^{\infty} 2v_n \cos[n(\varphi - \Psi^{\text{RP}})], \quad (1)$$

where φ denotes the azimuthal angle of a particle and Ψ^{RP} is the reaction plane azimuth (defined by the impact parameter vector). The Fourier coefficients,

$$v_n = \langle \cos[n(\varphi - \Psi^{\text{RP}})] \rangle, \quad (2)$$

are referred to as anisotropic flow of the n^{th} harmonic. By convention, v_1 , v_2 and v_3 are called “directed flow”, “elliptic flow”, and “triangular flow”, respectively. They

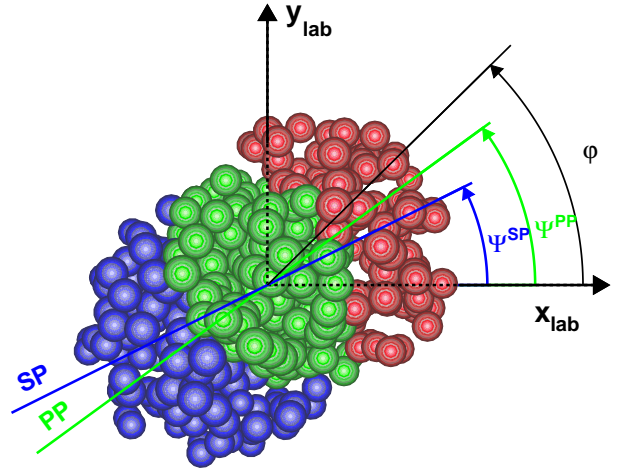


FIG. 1. (Color online) Schematic view of a two-nucleus collision in the transverse plane. The left nucleus is emerging from and the right one going into the page. Particles are produced in the overlap region (green-colored are the participant nucleons). The azimuthal angles of the spectator plane (Ψ^{SP}), the participant plane (Ψ^{PP}) and one of the produced particles (φ) are depicted here.

reflect the hydrodynamic response of the system to the initial geometry (and its fluctuations) of the participant zone [3].

In reality, the reaction plane is unknown, and more importantly, the initial-state fluctuations drive the anisotropic flow along the planes that differ from the reaction plane, the so-called flow symmetry planes or participant planes (Ψ_n^{PP}). Then the particle azimuthal distributions can be rewritten as

$$\frac{dN}{d\varphi} \propto 1 + \sum_{n=1}^{\infty} 2v_n \cos[n(\varphi - \Psi_n^{\text{PP}})]. \quad (3)$$

* zhiwanxu@physics.ucla.edu

† gwang@physics.ucla.edu

The meaning of the flow coefficients v_n changes from those in Eq. 2, but for simplicity of notations, the same symbols will be used, since in later discussions we will not determine the flow coefficients with the reaction plane. Anisotropic flow measurements relative to the participant plane are straightforward, as the flow itself can be used to estimate the corresponding flow plane. However, using the participant/flow plane also has its drawback – these planes become dependent on the kinematic region (rapidity and transverse momentum) of particles involved. This dependence is relatively weak, which still justifies the flow formalism of Eq. 3, but it needs to be taken into account to interpret high-precision flow measurements in modern experiments.

For clarity, we collect the definitions of different planes used in this paper below:

- Reaction plane (RP) is the plane spanned by the beam direction and the impact parameter vector. This plane is unique for every collision.
- Participant plane (PP) is defined by the initial density distribution. Subtle differences may exist, depending on, e.g., whether entropy or energy density is used as a weight, but these potentially small differences are not discussed in this paper. We assume that the properly constructed PPs define the development of anisotropic flow.
- Flow symmetry plane or flow plane (FP) determines the orientation of the corresponding harmonic anisotropic flow. It is assumed that FP coincides with the PP of the same harmonic (linear flow mode) or a proper combination of the lower harmonic PPs (nonlinear flow mode). With the nonlinear flow modes neglected, FP and PP are often used interchangeably.
- Event plane (EP) estimates the FP by analyzing the particle azimuthal distribution in a particular kinematic region. Owing to the finite number of particles involved in such an estimate, EP is subject to statistical fluctuations. The measurements obtained with EP have to be corrected for the event plane resolution [2], characterized by $\langle \cos[n(\Psi_n^{\text{EP}} - \Psi_n^{\text{FP}})] \rangle$. Ψ_n^{EP} is the azimuthal angle of the reconstructed n^{th} -harmonic flow vector, $\mathbf{Q}_n = (\sum_i^N w_i \cos(n\varphi_i), \sum_i^N w_i \sin(n\varphi_i))$, where w_i is the weight for each particle. For simplicity, we use unity weights in the event plane calculation.
- Spectator planes (SP) is determined by a sideward deflection of spectator nucleons, and is regarded as a better proxy for RP than FPs (determined by participants).

The objective of this paper is the flow-plane decorrelation in the (pseudo)rapidity direction. Decorrelation here means the deviation of a local flow plane from the value at the center-of-mass rapidity (y_{CM}), $\Delta\Psi(\eta) =$

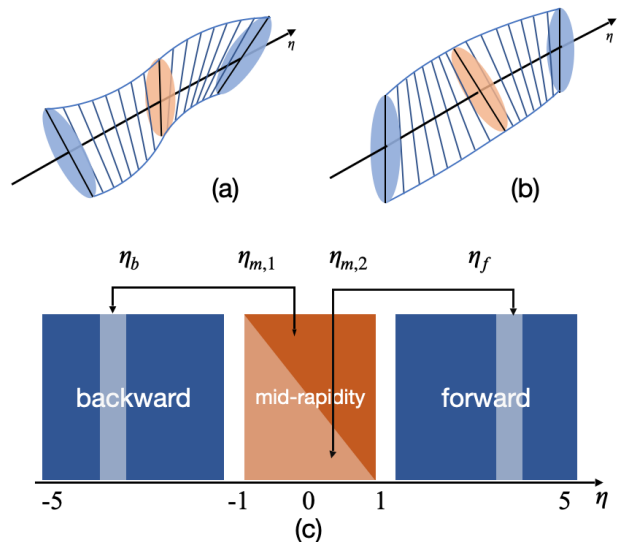


FIG. 2. (Color online) Schematic view of the “torque” or S-shaped (a), and the bow or C-shaped (b) decorrelation patterns in the longitudinal distribution of the flow plane angle. The ellipses indicate the transverse momentum distributions of the final-state particles. Panel (c) delimits the kinematic regions for the particles at mid-, forward, and backward pseudorapidities.

$\Psi(\eta) - \Psi(y_{\text{CM}})$. For simplicity, y_{CM} is set to zero for the symmetric collisions under study. In practice, we measure the relative tilt angles between the flow planes at backward, mid-, and forward rapidities. For concreteness we focus on the 2nd-harmonic flow. From event to event, two possible patterns arise from flow fluctuations: (a) when the flow plane angles at forward and backward pseudorapidities (Ψ_f and Ψ_b) fall on the opposite sides of the flow plane at midrapidity (Ψ_m) – the “torque” scenario, or S-shaped decorrelations, and (b) when Ψ_f and Ψ_b fall on the same side relative to Ψ_m – the “bow” scenario, or C-shaped decorrelations. These two cases are exemplified in panels (a) and (b) of Fig. 2, respectively.

The magnitude and pattern of the flow-plane decorrelation is extremely important, not only for the flow measurements (to be discussed in Sec. II), but also for understanding of the initial condition in the longitudinal direction. Flow-plane decorrelations can be caused by the torque effect [5], and more generally eccentricity decorrelations [6]. The mechanisms leading to the decorrelations also include hydrodynamic fluctuations in the QGP fluid [7] and glasma dynamics [8]. There also exists a phenomenological dynamical model of the initial states [9] that predicts the torque. We cannot exclude the possibility that the mechanisms causing the S-shaped decorrelations coexist with those originating the C-shaped ones in heavy-ion collisions. Therefore, experimental observables are only expected to measure the average effect and reveal the dominant decorrelation pattern.

A widely used measure of the longitudinal flow-plane decorrelation was introduced by the CMS Collabora-

tion [10]:

$$r_n(\eta) = \frac{\langle \cos[n(\varphi_{-\eta} - \Psi_f)] \rangle}{\langle \cos[n(\varphi_\eta - \Psi_f)] \rangle} \quad (4)$$

$$= \frac{\langle v_n(-\eta) \cos[n(\Psi_{-\eta} - \Psi_f)] \rangle}{\langle v_n(\eta) \cos[n(\Psi_\eta - \Psi_f)] \rangle}, \quad (5)$$

with $\eta > 0$. Ψ_f can be replaced with Ψ_b , if η and $-\eta$ are simultaneously swapped in the definition. In a symmetric collision without any decorrelation, one would expect that $v(\eta) = v(-\eta)$ and the ratio to be unity. But if a torque pattern is present, with Ψ_f serving as a reference point, the decorrelation effect would be stronger for the negative-rapidity region, and the ratio goes below unity. Experimental data show that r_2 indeed decreases with increasing η , and the deviation from unity is typically a few percent per unit pseudorapidity both at the LHC [10, 11] and RHIC [12]. Since both the flow-plane decorrelation and the flow-magnitude decorrelation can cause such a dependence of r_2 on η , efforts have been made to separate the two contributions [11, 13, 14]. However, before relating the observed $r_2(\eta)$ dependence to the flow-plane decorrelation, one has to examine an important physics background, the nonflow.

The nonflow effects are the correlations unrelated to the flow plane orientation or the initial geometry. Some nonflow effects are short-range in pseudorapidity, such as Coulomb and Bose-Einstein correlations (a few tenths of unit of rapidity), resonance decays, and intra-jet correlations (about one unit rapidity), whereas back-to-back jets could contribute to the long-range correlations spanning over several units of rapidity. Therefore, even with a sizable η gap between an event plane and the particles of interest, one can not completely eliminate nonflow contributions to v_2 or r_2 measurements. Nonetheless, the numerator of r_2 does involve a larger η gap and hence a smaller nonflow contribution than its denominator, leading to a ratio smaller than unity, similar to that caused by the S-shaped flow-plane decorrelation. On the other hand, the C-shaped decorrelation may also be faked in experimental observables by nonflow effects such as back-to-back jet correlations.

In Sec II, we use simple Monte Carlo simulations to demonstrate the impact of flow-plane decorrelations and nonflow on the v_2 measurements. Section III discusses the r_2 (and the closely related F_2 observable) analyses, and illustrates the possibilities of the η -differential measurements for a better interpretation of the results. We will show that nonflow effects tend to cause overestimation of F_2 , and to distort the $|\eta_{f(b)}|$ -dependence originally created by the flow-plane decorrelations. In Sec IV, we introduce a new four-plane observable, T_2 , which is free from most of the nonflow contribution and has very distinct expectations for different decorrelation patterns. In Sec V, the developed techniques are applied to the Au+Au events generated by the AMPT model. Finally in Sec VI, we summarize the findings and discuss the application of the new method to experimental data.

II. SIMPLE SIMULATIONS ON v_2

In elliptic flow measurements, it is a common practice to introduce a sizeable η gap between the event plane ($\Psi_{f(b)}$) and the particles of interest (φ_m) to suppress nonflow:

$$v_2\{\Psi_{f(b)}\} = \frac{\langle \cos[2(\varphi_m - \Psi_{f(b)})] \rangle}{\sqrt{\langle \cos[2(\Psi_f - \Psi_b)] \rangle}}, \quad (6)$$

where the denominator is the event plane resolution for $\Psi_{f(b)}$. Although both the numerator and the denominator are contaminated by nonflow, the latter is less affected because of a larger η gap between Ψ_f and Ψ_b . Therefore the effect of nonflow on $v_2\{\Psi_{f(b)}\}$ decreases with the increasing the η gap or $|\eta_{f(b)}|$.

When the S-shaped flow-plane decorrelation is present, both the numerator and the denominator in Eq. 6 are reduced by the finite tilt angles due to the η gaps, and the denominator is more influenced because it involves a larger η gap than the numerator. Therefore, the S-shaped decorrelation tends to drive $v_2\{\Psi_{f(b)}\}$ above $v_2\{\Psi_{\text{POI}}\}$, where Ψ_{POI} is the event plane determined in the same η region as the particles of interest (POI). To test this

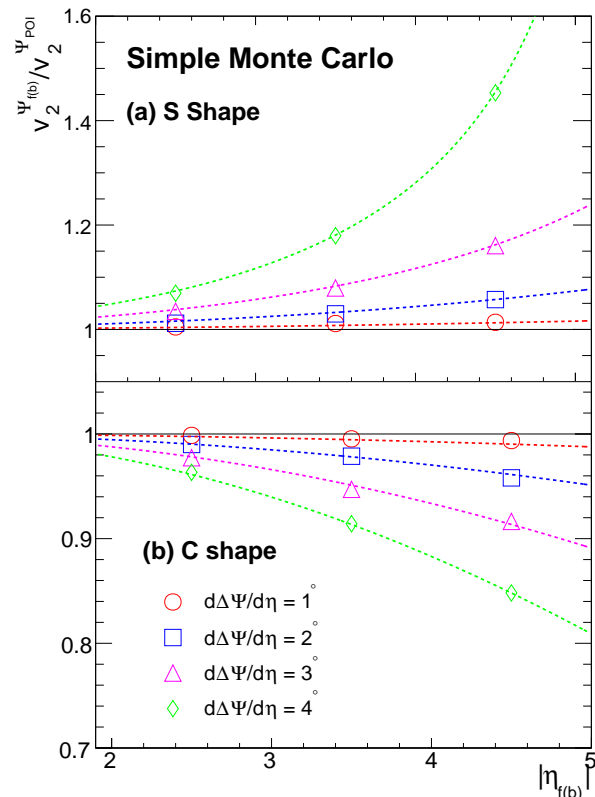


FIG. 3. (Color online) Simple Monte Carlo calculations of the ratio, $v_2\{\Psi_{f(b)}\}/v_2\{\Psi_{\text{POI}}\}$, without nonflow for the S-shaped (a) and the C-shaped (b) flow-plane decorrelations as a function of $|\eta_{f(b)}|$ and $\frac{d\Delta\Psi}{d\eta}$. The curves follow Eqs. (9) and (10).

speculation, we perform a simple Monte Carlo simulation, where the tilt angle, $\Delta\Psi(\eta)$, is a linear function of η , with a slope of $\frac{d\Delta\Psi}{d\eta} = 1^\circ, 2^\circ, 3^\circ$ or 4° :

$$\Delta\Psi(\eta) \equiv \Psi(\eta) - \Psi(0) = \frac{d\Delta\Psi}{d\eta} \eta. \quad (7)$$

In each event, the azimuthal angle of each particle has been assigned randomly according to the distribution of Eq. 3, with Ψ^{PP} replaced with $\Psi(\eta)$, and the η distribution is uniform over the scope of $(-5, 5)$. The particles of interest are within $|\eta| < 1$, and the $|\eta_{f(b)}|$ ranges used for calculations of Ψ_f and Ψ_b are taken from three bins: (2, 3), (3, 4) and (4, 5). For simplicity, the input v_2 is independent of η or transverse momentum (p_T), and the simulation does not include nonflow at this step. We implement a 30% flow fluctuation in all the following simple simulations, and observe no difference from results with zero fluctuation. Figure 3(a) shows that, as expected, the $v_2\{\Psi_{f(b)}\}/v_2\{\Psi_{\text{POI}}\}$ ratio is above unity, and increasing with both $|\eta_{f(b)}|$ and $\frac{d\Delta\Psi}{d\eta}$.

In the case of the C-shaped decorrelations, similar to Eq. 7, we assume

$$\Delta\Psi(\eta) = \frac{d\Delta\Psi}{d\eta} |\eta|, \quad (8)$$

with $\frac{d\Delta\Psi}{d\eta}$ still varying from 1° to 4° . Now that the tilt angle is symmetric around $\eta = 0$, the denominator in Eq. 6 is unchanged, and $v_2\{\Psi_{f(b)}\}$ tends to underestimate $v_2\{\Psi_{\text{POI}}\}$. Indeed, Fig. 3(b) shows that the $v_2\{\Psi_{f(b)}\}/v_2\{\Psi_{\text{POI}}\}$ ratio goes below unity, and decreasing with increasing $|\eta_{f(b)}|$ and $\frac{d\Delta\Psi}{d\eta}$ for the C-shaped case. The ratios for the S-shaped and the C-shaped scenarios can be well described, respectively, by

$$\frac{v_2\{\Psi_{f(b)}\}}{v_2\{\Psi_{\text{POI}}\}} = \frac{\cos(2\frac{d\Delta\Psi}{d\eta} |\eta_{f(b)}|)}{\sqrt{\cos(4\frac{d\Delta\Psi}{d\eta} |\eta_{f(b)}|)}} \quad (\text{S shape}), \quad (9)$$

$$\frac{v_2\{\Psi_{f(b)}\}}{v_2\{\Psi_{\text{POI}}\}} = \cos[2\frac{d\Delta\Psi}{d\eta} (|\eta_{f(b)}| - 0.5)] \quad (\text{C shape}). \quad (10)$$

We further implement some nonflow correlations in the simple simulation, by adding pairs of particles with the same azimuthal angle at different pseudorapidity locations. The η gap between the two particles follows a Gaussian distribution with zero mean and a width of 2 units of η . The fraction of paired-particles is set to 0, 15% and 30% to reflect the cases of no nonflow, weak nonflow and strong nonflow, respectively. The simulated $v_2\{\Psi_{f(b)}\}/v_2\{\Psi_{\text{POI}}\}$ ratio is shown in Fig. 4 as a function of $|\eta_{f(b)}|$ with different amounts of nonflow. Panel (a) displays the scenario without any decorrelation, where nonflow causes a decreasing trend, and the situation is more severe with stronger nonflow. Panel (b) gives an example with $\frac{d\Delta\Psi}{d\eta} = 2^\circ$ for the S-shaped and C-shaped flow-plane decorrelations. In both scenarios, nonflow pulls down the original trends, and in the case of the S-shaped decorrelation, the initially rising trend could even be reversed

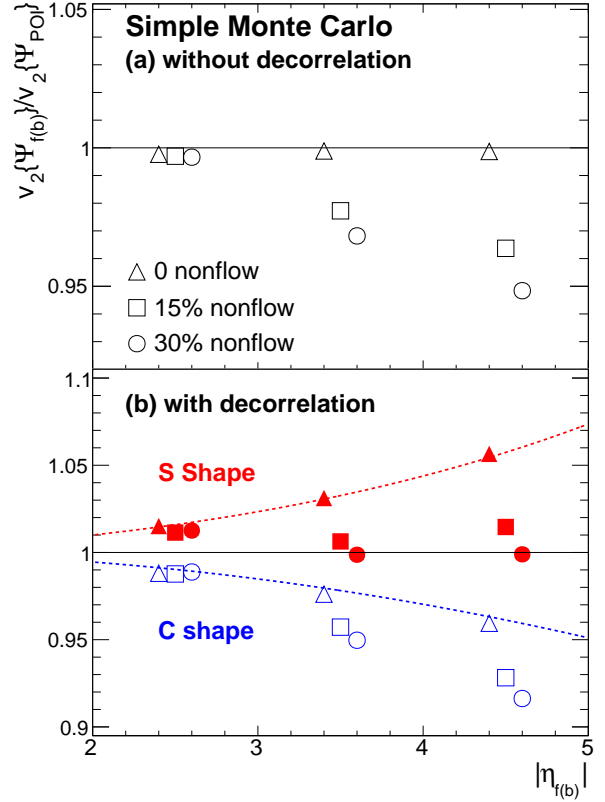


FIG. 4. (Color online) Simple Monte Carlo calculations of the $v_2\{\Psi_{f(b)}\}/v_2\{\Psi_{\text{POI}}\}$ ratio as a function of $|\eta_{f(b)}|$ with different amounts of nonflow. $\frac{d\Delta\Psi}{d\eta}$ is set to 2° for the S-shaped and the C-shaped flow-plane decorrelations. The curves follow Eqs. 9 and 10 without nonflow.

into a falling one. Therefore, the $v_2\{\Psi_{f(b)}\}/v_2\{\Psi_{\text{POI}}\}$ ratio alone lacks discernment of different decorrelation scenarios.

III. r_2 AND F_2

We define $r_2(\eta)$ based on Eq. 4 by setting $n = 2$. As suggested by Eq. 5, the deviation of r_2 from unity may originate from the decorrelations both in the flow-plane angles and in the v_2 magnitudes. Thus, we shall also examine the modified observable, r_2^Ψ [13], which is supposedly sensitive only to the flow-plane angles:

$$r_2^\Psi(\eta) = \frac{\langle \cos[2(\Psi_{-\eta} - \Psi_f)] \rangle}{\langle \cos[2(\Psi_\eta - \Psi_f)] \rangle}. \quad (11)$$

Experimentally as well as in model studies below, the dependence of $r_2^{(\Psi)}$ on η is almost linear, and the $F_2^{(\Psi)}$ slope is used to quantify the effect [10]:

$$r_2^{(\Psi)} = 1 - 2F_2^{(\Psi)}\eta. \quad (12)$$

We perform the linear- $\Delta\Psi(\eta)$ Monte Carlo simulation without nonflow to inspect the qualitative expectation

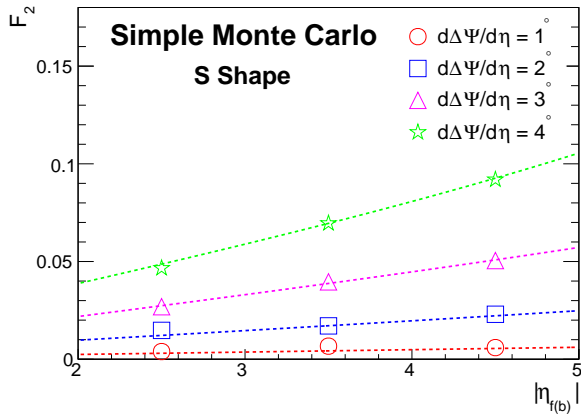


FIG. 5. (Color online) F_2 as a function of $|\eta_{f(b)}|$ and $\frac{d\Delta\Psi}{d\eta}$, from a simple Monte Carlo simulation for the S-shaped flow-plane decorrelation without nonflow. The curves reflect the analytical relation in Eq. 13.

of F_2 in the presence of the S-shaped flow-plane decorrelation. Note that in the C-shaped case, F_2 is zero by construction. In our simple simulations, F_2 and F_2^Ψ are always identical, so only the F_2 results are presented. Figure 5 depicts F_2 as a function of $|\eta_{f(b)}|$ and $\frac{d\Delta\Psi}{d\eta}$. F_2 increases with $\frac{d\Delta\Psi}{d\eta}$, since a larger tilt angle means a stronger torque. At first glance, it seems to be counter-intuitive that F_2 depends on the η location of the reference event plane, but the simulation actually reveals a simple mathematical relation:

$$1 - 2F_2\eta = \frac{\cos[2(\eta + |\eta_{f(b)}|)\frac{d\Delta\Psi}{d\eta}]}{\cos[2(\eta - |\eta_{f(b)}|)\frac{d\Delta\Psi}{d\eta}]}, \quad (13)$$

which yields $F_2 \approx 4(d\Delta\Psi/d\eta)^2|\eta_{f(b)}|$. Although in real collisions, the dependence of $\Delta\Psi$ on η may not be linear, our simple simulation catches the essence that the larger η gap between particles of interest and the reference event plane, the larger F_2 . Thus an experimental observation of the increasing $F_2(|\eta_{f(b)}|)$ trend might serve as an indication of the S-shaped flow-plane decorrelations, if there are no complications from other effects like nonflow.

In Fig. 6, nonflow contributions have been studied under the same framework as used for the $v_2\{\Psi_{f(b)}\}/v_2\{\Psi_{POI}\}$ ratio. Since the simple simulation results on F_2 are the same for the scenarios with no decorrelation and with the C-shaped decorrelation, we use one set of data points to present both of them in panel (a). In these two scenarios, nonflow can fake a finite F_2 value, which decreases with increasing $|\eta_{f(b)}|$. Furthermore, panel (b) shows that nonflow not only quantitatively increases the magnitude of F_2 for the S-shaped decorrelation, but could also qualitatively change its rising trend into a falling one vs $|\eta_{f(b)}|$. Therefore, F_2 cannot unambiguously distinguish and quantify different decorrelation scenarios.

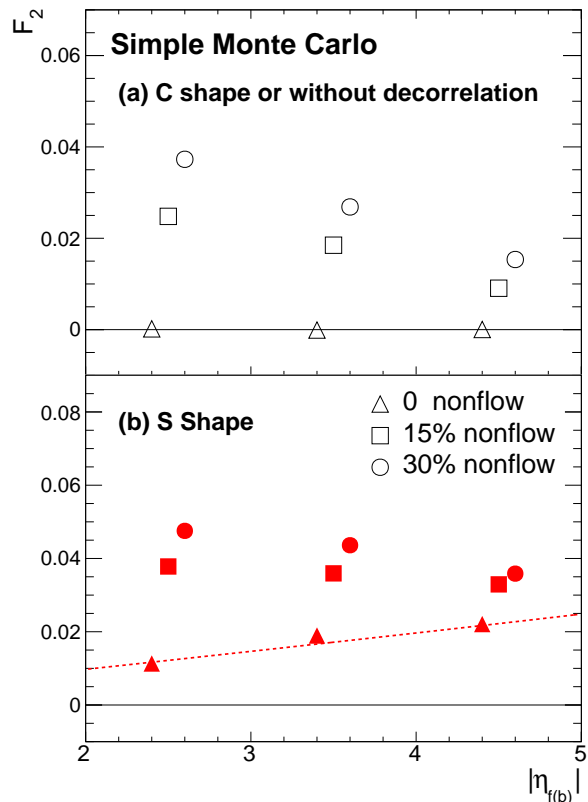


FIG. 6. (Color online) Simple Monte Carlo calculations of $F_2(|\eta_{f(b)}|)$ with different amounts of nonflow. $\frac{d\Delta\Psi}{d\eta}$ is set to 2° for the S-shaped and the C-shaped flow-plane decorrelations. The curve follows the ideal relation in Eq. 13 without nonflow.

IV. T_2 ANALYSES

In view of the significant nonflow contributions in $v_2\{\Psi_{f(b)}\}$ and F_2 analyses, we advocate a novel observable to probe the longitudinal flow-plane decorrelation:

$$T_2 = \frac{\langle\langle \sin 2(\Psi_f - \Psi_{m,1}) \sin 2(\Psi_b - \Psi_{m,2}) \rangle\rangle}{Res(\Psi_f)Res(\Psi_{m,1})Res(\Psi_b)Res(\Psi_{m,2})}, \quad (14)$$

where particles at midrapidities ($|\eta| < 1$) are randomly divided into two sub-events to form $\Psi_{m,1}$ and $\Psi_{m,2}$, as demonstrated in Fig. 2(c). The double bracket denotes ‘‘cumulant’’, and operates as follows:

$$\begin{aligned} & \langle\langle \sin(a - b) \sin(c - d) \rangle\rangle \\ & \equiv \langle \sin(a - b) \sin(c - d) \rangle - \frac{1}{2} \langle \cos(a - c) \rangle \langle \cos(b - d) \rangle \\ & \quad + \frac{1}{2} \langle \cos(a - d) \rangle \langle \cos(b - c) \rangle, \end{aligned} \quad (15)$$

the derivation of which is elaborated in Appendix A. The numerator of T_2 provides an intuitive way to tell whether Ψ_f and Ψ_b fall on the same side or the opposite sides of Ψ_m , and the denominator represents the product of the four event-plane resolutions. Taking into account the

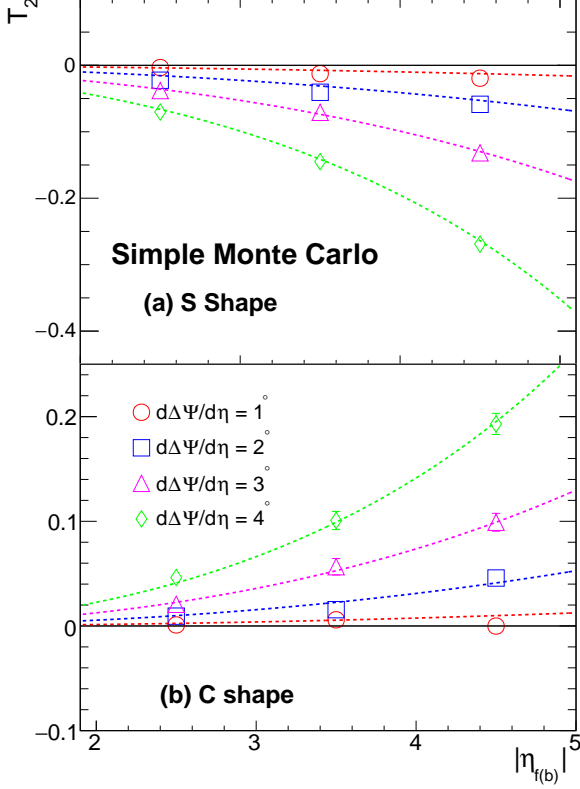


FIG. 7. (Color online) Simple Monte Carlo simulations of T_2 as a function of $|\eta_{f(b)}|$ and $\frac{d\Delta\Psi}{d\eta}$ for the S-shaped (a) and the C-shaped (b) flow-plane decorrelations without nonflow. The curves express Eqs. 17 and 18.

flow fluctuation contributions in the event plane resolution, we have

$$T_2 = \frac{\langle \sin 2(\Psi_f - \Psi_{m,1}) \sin 2(\Psi_b - \Psi_{m,2}) \rangle}{\langle \cos 2(\Psi_f - \Psi_{m,1}) \cos 2(\Psi_b - \Psi_{m,2}) \rangle} - \frac{\langle \cos 2(\Psi_f - \Psi_b) \rangle \langle \cos 2(\Psi_{m,1} - \Psi_{m,2}) \rangle}{2 \langle \cos 2(\Psi_f - \Psi_{m,1}) \rangle \langle \cos 2(\Psi_b - \Psi_{m,2}) \rangle} + \frac{1}{2}. \quad (16)$$

The generalization of the T_2 definition is also discussed in Appendix B.

If we ignore nonflow, a positive T_2 means a bow or a C-shaped decorrelation, and a negative T_2 signifies a torque or an S-shaped decorrelation. As done in the past, we shall exploit the linear- $\Delta\Psi(\eta)$ simulation without nonflow to learn the qualitative dependence of T_2 on $|\eta_{f(b)}|$ and $\frac{d\Delta\Psi}{d\eta}$ in different decorrelation patterns. With a specific $\frac{d\Delta\Psi}{d\eta}$, Fig. 7 shows a rapid decreasing trend of T_2 vs $|\eta_{f(b)}|$ for the S-shaped case in panel (a), and an increasing trend for the C-shaped case in panel (b). The

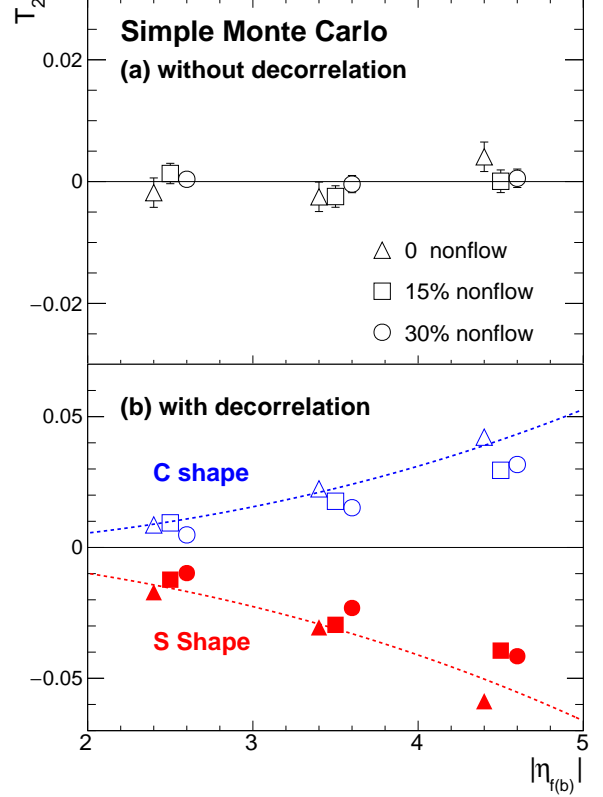


FIG. 8. (Color online) Simple Monte Carlo calculations of T_2 as a function of $|\eta_{f(b)}|$ with different amounts of nonflow. $\frac{d\Delta\Psi}{d\eta}$ is set to 2° for the S-shaped and the C-shaped flow-plane decorrelations. The curves manifest Eqs. 17 and 18 without nonflow.

simulated points obey the mathematical relations:

$$T_2 = -\frac{\sin^2(2\frac{d\Delta\Psi}{d\eta}|\eta_{f(b)}|) + \frac{1}{2}\cos(4\frac{d\Delta\Psi}{d\eta}|\eta_{f(b)}|)}{\cos^2(2\frac{d\Delta\Psi}{d\eta}|\eta_{f(b)}|)} + \frac{1}{2} = -\frac{1}{2}\tan^2(2\frac{d\Delta\Psi}{d\eta}|\eta_{f(b)}|) \text{ (S shape)}, \quad (17)$$

$$T_2 = \frac{\sin^2[2\frac{d\Delta\Psi}{d\eta}(|\eta_{f(b)}| - 0.5)] - \frac{1}{2}}{\cos^2[2\frac{d\Delta\Psi}{d\eta}(|\eta_{f(b)}| - 0.5)]} + \frac{1}{2} = \frac{1}{2}\tan^2[2\frac{d\Delta\Psi}{d\eta}(|\eta_{f(b)}| - 0.5)] \text{ (C shape)}. \quad (18)$$

Again, in reality, the tilt angle may not increase linearly with η gap, but the falling and rising trends of T_2 vs $|\eta_{f(b)}|$ should be solid expectations for the S-shaped and the C-shaped decorrelations, respectively.

In $v_2\{\Psi_{f(b)}\}$ and F_2 analyses, the core element is a cosine function that yields large values close to one in strong-nonflow scenarios. Conversely, T_2 uses the cumulant of a sine function that gives close-to-zero nonflow contributions. Nonflow studies on T_2 are presented in Fig. 8 with the same procedure as before. Panel (a) shows that for the scenario without any decorrelation,

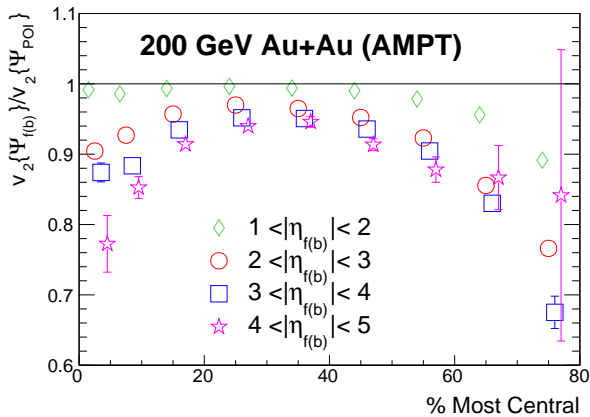


FIG. 9. (Color online) AMPT calculations of the $|\eta_{f(b)}|$ dependence of the $v_2\{\Psi_{f(b)}\}/v_2\{\Psi_{POI}\}$ ratio in different centrality intervals of Au+Au collisions at $\sqrt{s_{NN}} = 200$ GeV. Results using Ψ_f and Ψ_b are combined. Some points are staggered horizontally to improve visibility.

the T_2 results are always consistent with zero, even with a strong nonflow input. Therefore, nonflow can not fake a finite signal of T_2 . Panel (b) shows that for the scenarios with the C-shaped and the S-shaped decorrelations, the T_2 magnitude could be slightly reduced by nonflow, but the original trends are not changed vs $|\eta_{f(b)}|$.

V. AMPT STUDIES

We shall test the aforementioned methodology with more realistic events, simulated by the AMPT model [15]. AMPT is a hybrid transport event generator, and describes four major stages of a high-energy heavy-ion collision: the initial conditions, the partonic evolution, the hadronization, and the hadronic interactions. For the initial conditions, AMPT uses the spatial and momentum distributions of minijet partons and excited soft strings, as adopted in the Heavy Ion Jet Interaction Generator (HIJING) [16]. Then Zhang's parton cascade (ZPC) [17] is deployed to manage the partonic evolution, determined by the two-body parton-parton elastic scattering. At the end of the partonic evolution, the hadronization is implemented via the spatial quark coalescence. Finally, the hadronic interactions are modelled by A Relativistic Transport calculations (ART) [18]. The string-melting (SM) version of AMPT reasonably well reproduces particle spectra and elliptic flow in Au+Au collisions at $\sqrt{s_{NN}} = 200$ GeV and Pb+Pb collisions at 2.76 TeV [19]. In this study, Au+Au collisions at 200 GeV are simulated by the SM version v2.25t4cu of AMPT.

In the following analyses of the AMPT events, we only select π^\pm , K^\pm , p and \bar{p} with $0.15 < p_T < 2$ GeV/c. φ_m and Ψ_m are delimited with $|\eta| < 1$, and Ψ_f and Ψ_b are reconstructed with particles within $2 < \eta < 5$ and $-5 < \eta < -2$, respectively. With the expectations from

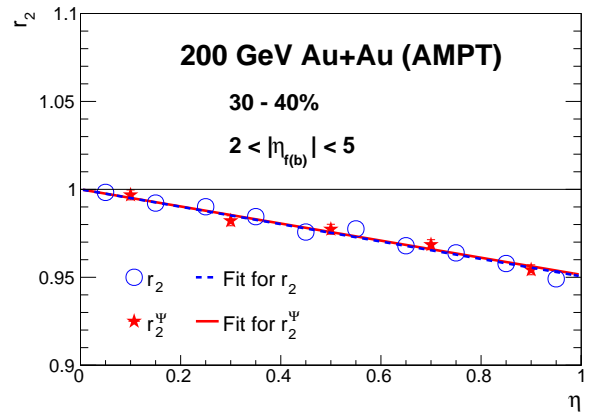


FIG. 10. (Color online) $r_2(\eta)$ and $r_2^\Psi(\eta)$ in 30-40% Au+Au collisions at $\sqrt{s_{NN}} = 200$ GeV, simulated by AMPT. Results using Ψ_f and Ψ_b are combined. The straight-line fits to the r_2 and r_2^Ψ points extract the corresponding F_2 of $(2.47 \pm 0.11) \times 10^{-2}$ and F_2^Ψ of $(2.43 \pm 0.11) \times 10^{-2}$.

nonflow and the scenarios of flow-plane decorrelations in mind (see Figs. 3 and 4), we examine the $|\eta_{f(b)}|$ dependence of the $v_2\{\Psi_{f(b)}\}/v_2\{\Psi_{POI}\}$ ratio in AMPT. Figure 9 shows the AMPT calculations of this ratio for four $|\eta_{f(b)}|$ bins in different centrality intervals of Au+Au collisions at $\sqrt{s_{NN}} = 200$ GeV. Within each centrality bin, $v_2\{\Psi_{f(b)}\}/v_2\{\Psi_{POI}\}$ displays a decreasing trend with the increasing η gap, excluding the S-shaped decorrelation from the dominant underlying mechanisms. Both nonflow and the C-shaped decorrelation could induce such a decreasing trend in the v_2 ratio, and we cannot yet discern the two scenarios using this observable.

Next, the AMPT results of $r_2(\eta)$ and $r_2^\Psi(\eta)$ are compared in Fig. 10 for 30-40% Au+Au collisions at 200 GeV. As mentioned earlier, Ψ_f can be replaced with Ψ_b in the r_2 definition, with η and $-\eta$ simultaneously exchanged. The two sets of results have been combined to gain better

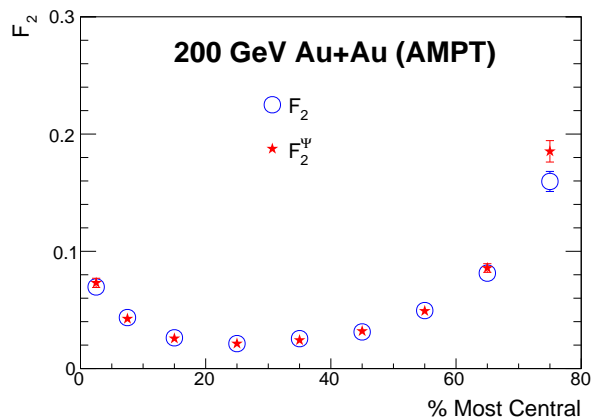


FIG. 11. (Color online) F_2 and F_2^Ψ as functions of centrality in Au+Au collisions at $\sqrt{s_{NN}} = 200$ GeV from AMPT.

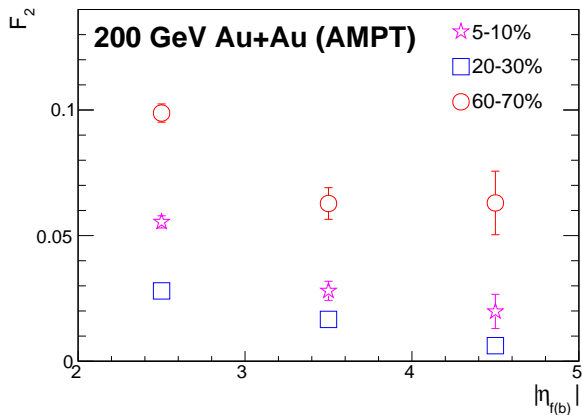


FIG. 12. (Color online) AMPT calculations of F_2 versus $|\eta_{f(b)}|$ for three selected centrality ranges in Au+Au collisions at $\sqrt{s_{NN}} = 200$ GeV.

statistics. Both r_2 and r_2^Ψ show a linear trend decreasing as η increases, seemingly indicating a torque in the flow-plane decorrelation at midrapidities. The linear fits render the very close values of $F_2 = (2.47 \pm 0.11) \times 10^{-2}$ and $F_2^\Psi = (2.43 \pm 0.11) \times 10^{-2}$, which implies a marginal contribution of v_2 -magnitude decorrelations at midrapidities in AMPT events.

Figure 11 presents the AMPT calculations of F_2 and F_2^Ψ as functions of centrality. The two quantities are very close to each other in most centrality bins, with a potential deviation in 70-80% collisions. Thereafter, we will focus on F_2 . The magnitude of F_2 is about 2.5% in the 10-50% centrality range, and becomes larger in more central and more peripheral events. Before attributing the finite F_2 values to the flow-plane decorrelation, one should note that such a centrality dependence could be a reflection of nonflow effects. Nonflow contributions are positive in F_2 , and become more pronounced in peripheral collisions where multiplicity is low and in central collisions where v_2 is small. This caveat also applies to experimental data [12, 20] that show F_2 features similar to these AMPT simulations.

The qualitative expectation from the simple Monte Carlo simulation (see Figs. 5 and 6) motivates the differential measurements of F_2 with respect to $|\eta_{f(b)}|$. Figure 12 delineates AMPT calculations of F_2 as a function of $|\eta_{f(b)}|$ for three selected centrality bins in Au+Au collisions at 200 GeV. The F_2 values are positive for all the cases under study, consistent with the S-shaped decorrelation. However, the $|\eta_{f(b)}|$ dependence shows a falling trend in each centrality interval, in contrast to the rising trend expected for the torque alone. Therefore, the contribution of the S-shaped flow-plane decorrelation in these F_2 values, if any, must have been dominated by nonflow effects, which are also positive, and decrease with increasing $|\eta_{f(b)}|$.

Finally, Fig. 13 depicts the T_2 values for all the centrality intervals under study in the AMPT events of Au+Au

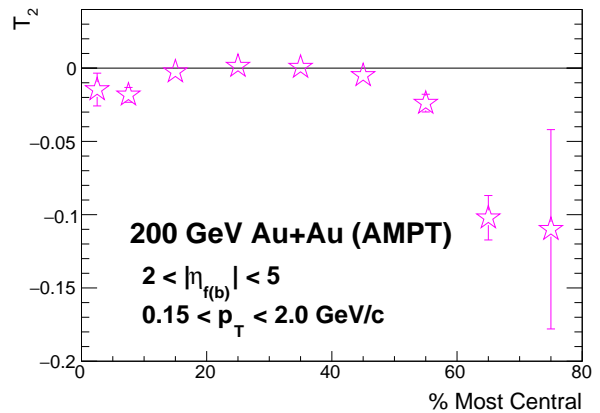


FIG. 13. (Color online) Centrality dependence of T_2 in AMPT events of Au+Au collisions at $\sqrt{s_{NN}} = 200$ GeV. The $|\eta_{f(b)}|$ range is (2, 5) for Ψ_f and Ψ_b .

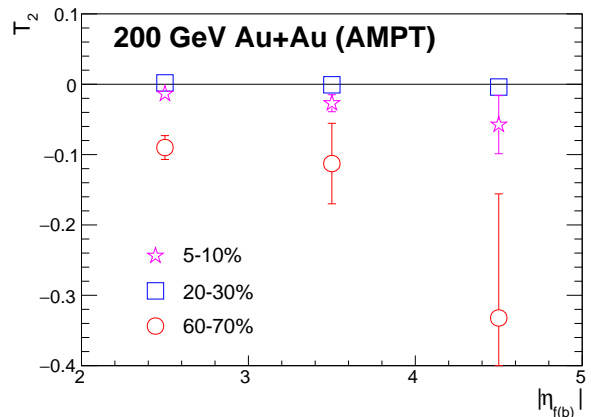


FIG. 14. (Color online) T_2 dependence on $|\eta_{f(b)}|$ for three selected centrality ranges in AMPT events of Au+Au collisions at $\sqrt{s_{NN}} = 200$ GeV.

collisions at 200 GeV. For the 10 – 50% centrality range, T_2 is consistent with zero, indicating no apparent flow-plane decorrelation. In more central or more peripheral events, T_2 falls negative, supporting the picture of a torque or the S-shaped decorrelation. Note that when the tilt angle between Ψ_m and $\Psi_{f(b)}$ becomes large, the denominator of T_2 significantly under-estimates the product of the event-plane resolutions, which in turn will blow up the magnitudes of both T_2 and its statistical uncertainty. This partially attributes to the large T_2 magnitudes and the large error bars in peripheral collisions. The bright side is that this effect does not change the sign of T_2 , because the denominator is always positive by symmetry.

The AMPT results of T_2 as a function of $|\eta_{f(b)}|$ are plotted in Fig. 14 for three selected centrality bins in Au+Au collisions at 200 GeV. For the 20 – 30% centrality range, T_2 is always consistent with zero, whereas for

TABLE I. AMPT results of T_2 and F_2 as well as the corresponding tilt angles ($\frac{d\Delta\Psi}{d\eta}$) versus centrality in Au+Au collisions at 200 GeV. $\frac{d\Delta\Psi}{d\eta}$ is extracted using Eqs. 13, 17 and 18 without nonflow. For the tilt angles from T_2 , a minus sign is added, if the decorrelation is C-shaped.

% central	F_2 (%)	T_2 (%)	$\frac{d\Delta\Psi}{d\eta}\{F_2\}$ ($^\circ$)	$\frac{d\Delta\Psi}{d\eta}\{T_2\}$ ($^\circ$)
0-5	7.0 (0.4)	-1.5 (1.1)	4.26 (0.13)	1.3 (0.9)
5-10	4.3 (0.2)	-1.8 (0.5)	3.37 (0.09)	1.7 (0.2)
10-20	2.6 (0.1)	-0.2 (0.2)	2.61 (0.06)	0.5 (0.4)
20-30	2.1 (0.1)	0.1 (0.2)	2.35 (0.06)	-0.4 (0.5)
30-40	2.6 (0.1)	0.1 (0.2)	2.57 (0.06)	-0.2 (0.6)
40-50	3.1 (0.1)	-0.5 (0.3)	2.84 (0.06)	0.8 (0.3)
50-60	4.9 (0.2)	-2.4 (0.6)	3.57 (0.08)	1.9 (0.2)
60-70	8.1 (0.4)	-10.2 (1.5)	4.58 (0.10)	3.8 (0.3)
70-80	16.0 (0.9)	-11.0 (6.8)	6.42 (0.17)	3.6 (1.7)

5 – 10% and 60 – 70% collisions, there seem to be decreasing trends due to a torque, although the statistical uncertainties become large at increased $|\eta_{f(b)}|$. Therefore, both the sign and the $|\eta_{f(b)}|$ -dependence of T_2 confirm the S-shaped longitudinal decorrelation in central and peripheral AMPT events.

A comparison between F_2 and T_2 is possible, if we neglect nonflow effects for the moment, and use Eqs. 13, 17 and 18 to extract the tilt angles from these two observables. Table I lists the values of F_2 and T_2 as functions of centrality from Figs. 11 and 13, as well as the extracted tilt angles. The average $|\eta_{f(b)}|$ is around 3.2 with a weak centrality dependence. In general, the tilt angles obtained from F_2 have larger magnitudes than those from T_2 , since the former is subject to severe positive nonflow contributions, whereas the latter is reduced by nonflow. The true $\frac{d\Delta\Psi}{d\eta}$ should lie between them, somewhere close to the value from T_2 .

VI. CONCLUSIONS

The flow-plane azimuthal decorrelations provide important input to the initial condition and the system evolution of heavy-ion collisions in the longitudinal dimension. We have explored three analyses that may be sensitive to such decorrelations: $v_2\{\Psi_{f(b)}\}/v_2\{\Psi_{POI}\}$, $F_2^{(\Psi)}$ and T_2 . Using simple Monte Carlo simulations with a constant $\frac{d\Delta\Psi}{d\eta}$ slope, we have learned the impacts of decorrelation and nonflow on these observables as functions of $|\eta_{f(b)}|$.

- In the absence of nonflow, the $v_2\{\Psi_{f(b)}\}/v_2\{\Psi_{POI}\}$ ratio will increase(decrease) with increasing $|\eta_{f(b)}|$, if the decorrelation is S-shaped(C-shaped). However, nonflow tends to pull down the trend, and could cause a falling trend even with the S-shaped decorrelation.
- Without nonflow, F_2 is zero in the case of the C-shaped decorrelation or no decorrelations, and

is positive, increasing with $|\eta_{f(b)}|$ in the S-shaped case. Again, nonflow could force a decreasing trend regardless of whether the decorrelation is a torque or a bow.

- $T_2(|\eta_{f(b)}|)$ is expected to distinguish the C-shaped and the S-shaped decorrelation patterns with opposite trends. Nonflow could slightly reduce the magnitude of T_2 , but is unlikely to fake a decorrelation or change the pertinent trend.

We have further applied the aforementioned methods to the AMPT events of Au+Au collisions at $\sqrt{s_{NN}} = 200$ GeV. The findings are summarized in the following.

- For each centrality interval under study, the $v_2\{\Psi_{f(b)}\}/v_2\{\Psi_{POI}\}$ ratio decreases with increasing $|\eta_{f(b)}|$, which means that the S-shaped decorrelation cannot be the dominant underlying mechanism for this observable. This approach is unable to separate nonflow from the C-shaped decorrelation.
- F_2 and $F_2^{(\Psi)}$ are very close to each other in most cases, indicating a negligible v_2 -magnitude decorrelation in AMPT. It is of interest to see if that is also true in experimental data.
- Although the positive sign of $F_2^{(\Psi)}$ seems to evidence the torque in AMPT, nonflow contributions cast a shadow over this interpretation, with the decreasing trend of $F_2(|\eta_{f(b)}|)$.
- The novel observable, T_2 , suppresses nonflow with the sine function and the cumulant treatment. T_2 is consistent with no decorrelation for 10 – 50% AMPT events of Au+Au at 200 GeV, and supports the S-shaped decorrelation picture in 0 – 10% and 50 – 80% collisions, with both the sign and the $|\eta_{f(b)}|$ -dependence.

In short, the proposed T_2 observable suppresses nonflow contributions, and is sensitive to dynamics of the decorrelation patterns tracing back to the initial participant matter. We look forward to the application of this new method to the real data analyses.

ACKNOWLEDGMENTS

We thank Maowu Nie, Jiangyong Jia, Aihong Tang, ShinIchi Esumi and Mike Lisa for the fruitful discussions. Z. Xu, X. Wu, G. Wang and H. Huang are supported by the U.S. Department of Energy under Grant No. DE-FG02-88ER40424. C. Sword and S. Voloshin are supported by the U.S. Department of Energy Office of Science, Office of Nuclear Physics under Award No. DE-FG02-92ER40713.

Appendix A: Cumulant of four-angle correlations

The two-variable cumulant of an observable, $f = xy$, is defined as

$$\langle\langle xy \rangle\rangle \equiv \langle xy \rangle - \langle x \rangle \langle y \rangle. \quad (\text{A1})$$

The first term computes the average of the product, accounting for correlations between x and y , while the second gives the product of the averages, keeping x and y independent of each other. A zero cumulant means that x and y are independent with no correlation. The T_2 observable involves four azimuthal angles, and therefore we shall derive the four-variable cumulant, which subtracts all lower-order correlations:

$$\begin{aligned} \langle\langle xyzt \rangle\rangle &\equiv \langle xyzt \rangle - \langle\langle xyz \rangle\rangle \langle t \rangle - \langle\langle xyt \rangle\rangle \langle z \rangle \\ &\quad - \langle\langle xzt \rangle\rangle \langle y \rangle - \langle\langle yzt \rangle\rangle \langle x \rangle - \langle\langle xy \rangle\rangle \langle\langle zt \rangle\rangle \\ &\quad - \langle\langle xz \rangle\rangle \langle\langle yt \rangle\rangle - \langle\langle xt \rangle\rangle \langle\langle yz \rangle\rangle \\ &\quad - \langle x \rangle \langle y \rangle \langle z \rangle \langle t \rangle. \end{aligned} \quad (\text{A2})$$

In principle, we should obtain the three-variable cumulants before calculating the four-variable cumulant. However, in the case of T_2 , all the variables can be expressed as a sine or cosine function of an azimuthal angle, and we can force $\langle x \rangle = \langle y \rangle = \langle z \rangle = \langle t \rangle = 0$ in the data analyses, e.g., via the shifting method [21]. Thus, Eq. A2 is simplified to

$$\langle\langle xyzt \rangle\rangle = \langle xyzt \rangle - \langle xy \rangle \langle zt \rangle - \langle xz \rangle \langle yt \rangle - \langle xt \rangle \langle yz \rangle. \quad (\text{A3})$$

The numerator of T_2 can be expanded into four terms:

$$\begin{aligned} &\sin(a-b)\sin(c-d) \\ &= \sin(a)\cos(b)\sin(c)\cos(d) \\ &\quad - \sin(a)\cos(b)\sin(d)\cos(c) \\ &\quad - \sin(b)\cos(a)\sin(c)\cos(d) \\ &\quad + \sin(b)\cos(a)\sin(d)\cos(c). \end{aligned} \quad (\text{A4})$$

We put the first term into Eq. A3 as an example,

$$\begin{aligned} &\langle\langle \sin(a)\cos(b)\sin(c)\cos(d) \rangle\rangle \\ &= \langle\sin(a)\cos(b)\sin(c)\cos(d)\rangle \\ &\quad - \langle\sin(a)\sin(c)\rangle \langle\cos(b)\cos(d)\rangle, \end{aligned} \quad (\text{A5})$$

where terms such as $\langle\sin(a)\cos(b)\rangle$ vanish in symmetric heavy-ion collisions. Using the product-to-sum formulas, we have

$$\begin{aligned} &\langle\sin(a)\sin(c)\rangle \langle\cos(b)\cos(d)\rangle \\ &= \frac{1}{4} [\langle\cos(a-c)\rangle \langle\cos(b-d)\rangle \\ &\quad + \langle\cos(a+c)\rangle \langle\cos(b+d)\rangle \\ &\quad - \langle\cos(a+c)\rangle \langle\cos(b-d)\rangle \\ &\quad - \langle\cos(a-c)\rangle \langle\cos(b+d)\rangle]. \end{aligned} \quad (\text{A6})$$

Only the cosines with arguments of the angle difference are independent of the coordinate system, and may render finite averages. Hence Eq. A5 becomes

$$\begin{aligned} &\langle\langle \sin(a)\cos(b)\sin(c)\cos(d) \rangle\rangle \\ &= \langle\sin(a)\cos(b)\sin(c)\cos(d)\rangle \\ &\quad - \frac{1}{4} \langle\cos(a-c)\rangle \langle\cos(b-d)\rangle. \end{aligned} \quad (\text{A7})$$

We follow the same procedure for the other three terms in Eq. A4 and obtain

$$\begin{aligned} &\langle\langle \sin(a-b)\sin(c-d) \rangle\rangle \\ &\equiv \langle\sin(a-b)\sin(c-d)\rangle - \frac{1}{2} \langle\cos(a-c)\rangle \langle\cos(b-d)\rangle \\ &\quad + \frac{1}{2} \langle\cos(a-d)\rangle \langle\cos(b-c)\rangle. \end{aligned} \quad (\text{A8})$$

Appendix B: Generalization of T_2

In the T_2 analyses in Sec. IV, we randomly split particles within $|\eta| < 1$ into two sub-events, and reconstruct $\Psi_{m,1}$ and $\Psi_{m,2}$ based on them. By this means, $\Psi_{m,1}$ and $\Psi_{m,2}$ are indistinguishable, sharing the same kinematic region, bearing the same event plane resolution, and tilting in the same way. In general, $\Psi_{m,1}$ and $\Psi_{m,2}$ could come from different η ranges, e.g., with $-1 < \eta_{m,1} < 0$ and $0 < \eta_{m,2} < 1$. Accordingly, the definition of T_2 is not unique any more, with a few possible combinations. For example, we can define

$$T_{2(I)} = \frac{\langle\langle \sin 2(\Psi_f - \Psi_{m,2}) \sin 2(\Psi_b - \Psi_{m,1}) \rangle\rangle}{\langle\cos 2(\Psi_f - \Psi_{m,2})\rangle \langle\cos 2(\Psi_b - \Psi_{m,1})\rangle}, \quad (\text{B1})$$

and within the frame work of the simple Monte Carlo simulation, where the tilt angle linearly increases with η gap, we have

$$T_{2(I)} = -\frac{1}{2} \tan^2 \left[2 \frac{d\Delta\Psi}{d\eta} (|\eta_{f(b)}| - 0.5) \right] \text{ (S shape)}, \quad (\text{B2})$$

$$T_{2(I)} = \frac{1}{2} \tan^2 \left[2 \frac{d\Delta\Psi}{d\eta} (|\eta_{f(b)}| - 0.5) \right] \text{ (C shape)}. \quad (\text{B3})$$

We can switch $\Psi_{m,1}$ and $\Psi_{m,2}$ in $T_{2(I)}$ to define a new observable

$$T_{2(II)} = \frac{\langle\langle \sin 2(\Psi_f - \Psi_{m,1}) \sin 2(\Psi_b - \Psi_{m,2}) \rangle\rangle}{\langle\cos 2(\Psi_f - \Psi_{m,1})\rangle \langle\cos 2(\Psi_b - \Psi_{m,2})\rangle}, \quad (\text{B4})$$

and with the constant $\frac{d\Delta\Psi}{d\eta}$, we have

$$T_{2(II)} = -\frac{1}{2} \tan^2 \left[2 \frac{d\Delta\Psi}{d\eta} (|\eta_{f(b)}| + 0.5) \right] \text{ (S shape)}, \quad (\text{B5})$$

$$T_{2(II)} = \frac{1}{2} \tan^2 \left[2 \frac{d\Delta\Psi}{d\eta} (|\eta_{f(b)}| - 0.5) \right] \text{ (C shape)}. \quad (\text{B6})$$

A third type of T_2 observable can be defined as

$$T_{2(III)} = \frac{\langle\langle \sin 2(\Psi_f - \Psi_b) \sin 2(\Psi_{m,1} - \Psi_{m,2}) \rangle\rangle}{\langle\cos 2(\Psi_f - \Psi_b)\rangle \langle\cos 2(\Psi_{m,1} - \Psi_{m,2})\rangle}, \quad (\text{B7})$$

which is zero for the C-shaped decorrelation. With the constant $\frac{d\Delta\Psi}{d\eta}$, the expectation from the S-shaped case is

$$T_{2(III)} = -\frac{1}{2} \tan\left(2\frac{d\Delta\Psi}{d\eta}\right) \tan\left(4\frac{d\Delta\Psi}{d\eta} |\eta_{f(b)}|\right). \quad (\text{B8})$$

-
- [1] S. Voloshin and Y. Zhang, Z. Phys. C **70**, 665 (1996).
[2] A. M. Poskanzer and S. A. Voloshin, Phys. Rev. C **58**, 1671 (1998).
[3] U. Heinz and R. Snellings, Ann. Rev. Nucl. Part. Sci. **63**, 123 (2013).
[4] R. J. Glauber and G. Matthiae, Nucl. Phys. B **21**, 135 (1970).
[5] P. Bozek, W. Broniowski, and J. Moreira, Phys. Rev. C **83**, 034911 (2011).
[6] A. Behera, M. Nie, and J. Jia, (2020), Phys. Rev. Research **2**, 023362 (2020).
[7] L.-G. Pang, G.-Y. Qin, V. Roy, X.-N. Wang, and G.-L. Ma, Phys. Rev. C **91**, 044904 (2015).
[8] B. Schenke and S. Schlichting, Phys. Rev. C **94**, 044907 (2016).
[9] Shen, Chun and Schenke, Bjorn, Phys. Rev. C **97**, 024907 (2018).
[10] V. Khachatryan *et al.* [CMS Collaboration], Phys. Rev. C **92**, 034911 (2015).
[11] M. Aaboud *et al.* [ATLAS Collaboration], Eur. Phys. J. C **76**, 142 (2017).
[12] M. Nie [STAR Collaboration], arXiv:2005.03252.
[13] P. Bozek and W. Broniowski, Phys. Rev. C **97**, 034913 (2018).
[14] A. Sakai, K. Murase, T. Hirano, arXiv:2003.13496.
[15] Z.-W. Lin, C.M. Ko, B.-A. Li, B. Zhang, S. Pal, Phys. Rev. C **72**, 064901 (2005).
[16] X.-N. Wang and M. Gyulassy, Phys. Rev. D **44**, 3501 (1991).
[17] B. Zhang, Comput. Phys. Commun. **109**, 193 (1998).
[18] B. A. Li and C. M. Ko, Phys. Rev. C **52**, 2037 (1995).
[19] Zi-Wei Lin, Phys. Rev. C **90**, 014904 (2014).
[20] V. Khachatryan *et al.* [CMS Collaboration], Phys. Rev. C **92**, 034911 (2015).
[21] J. Barrette *et al.* [E877 Collaboration], Phys. Rev. C **56**, 3254 (1997).